Chemical Tuning of Metal Nanocatalysts Interface for ORR Electrocatalysis

Quentin Lenne, Alice Mattiuzzi, Ivan Jabin, Jonathan Hamon, Yann R Leroux, Corinne Lagrost

RESEARCH ARTICLE

Editor's Choice

ADVANCED MATERIALS INTERFACES

www.advmatinterfaces.de

Chemical Tuning of Metal Nanocatalysts Interface for ORR Electrocatalysis

Quentin Lenne, Alice Mattiuzzi, Ivan Jabin, Jonathan Hamon, Yann R. Leroux, and Corinne Lagrost**

A series of surface-functionalized gold nanocatalysts are synthesized. Through diazonium chemistry, calix[4]arene molecules are grafted at the gold surface. Sharing the same anchoring function and a common backbone, the calix[4]arene ligands possess distinct terminal chemical functions where the length, hydrophobic nature, and oxygen affinity are varied. Thanks to the versatility of the calix[4]arene platform, this paper only focuses on the molecular tuning of the solid/liquid interface through the change of the tail groups while electronic effects that are regulated by the anchoring function will be similar for all catalysts. Electrocatalytic tests demonstrate the influence of the tails group on the oxygen reduction reaction performances, including efficiency, selectivity, and durability. Beyond a pure geometric steric effect, it is shown that chemical properties of the ligands can effectively tune the interactions between the metallic catalyst and the electrolyte and reactants.

1. Introduction

Up to recently, the deliberate molecular functionalization of metal-based catalysts was limited to molecular complexes in homogeneous catalysis where organic ligands can steer the activity and selectivity of metal centers.[1] In this field, a thorough design of the environment surrounding the active metal site is often used to leverage more the chemical reactivity, i.e., both kinetics and reactions mechanism. Beyond a simple alteration or availability of the active catalytic sites, the presence of ligands could lead to a steric or electronic control of the catalytic site as well as a metal–ligand cooperativity introducing new reaction pathways. In contrast, in the field of heterogeneous catalysis, chemical reactivity and/or selectivity are commonly only tuned through catalytic sites alteration or by increasing their relative number thanks to nanostructuring. This is notably the case with nanoparticle catalysis, which is of primary importance in many heterogeneous reactions due to the inherent high surface to mass ratio and controllable surface structure of the nanocatalysts. Herein the manipulations of size, of shape or of composition by topmost engineering with foreign metals of the nanomaterials is currently exploited to tune the reactivity and selectivity of the catalytic systems.[2–7] Such manipulations are very often achieved thanks to small molecules or polymers acting as capping agents able to regulate the size and shape during the synthesis and to prevent from aggregation.[8] But the organic capping agents are generally undesired at the catalytic surface because they are considered as inert species hiding the active sites on the nanoparticle catalyst. Thus, additional effort has to be made for the removal of organic ligands prior to use, without altering the material structure or morphology.[5,7,9–11] However, the promoting effects of ligands on heterogeneous catalysts have recently emerged, and a number of studies has shown that surface ligands can actually enhance the selectivity, activity and/or durability, notably in important electrocatalytic reactions including hydrogen evolution reaction (HER), carbon dioxide reduction reaction (CO_2RR) or oxygen reduction reaction (ORR).[12-16]

The reasons why the organic modifiers can tune the electrocatalytic activity are critical questions to address in order to rationalize their design for taking better benefit of this strategy. Electronic and steric effects of organic ligands are generally considered and are the most widely discussed.[14,16] Electronic effect is mainly due to the anchoring moiety which could influence the local electronic structure of the surface through metal–ligand interaction. The steric effect corresponds to the selective blocking of metal surface by the ligand at the surface due its geometry and/or size, hence mostly ruled by its

Q. Lenne, Y. R. Leroux, C. Lagrost
CNRS
Univ. Rennes
ISCR–UMR 6226, Rennes 35000, France
E-mail: yann.leroux@univ-rennes1.fr; corinne.lagrost@univ-rennes1.fr
A. Mattiuzzi
X4C
48 rue Auguste Piccard, Gosselies 6041, Belgium
I. Jabin
Laboratoire de Chimie Organique
Université libre de Bruxelles (ULB)
CP 160/06, Avenue F.D. Roosevelt 50, Brussels 1050, Belgium
J. Hamon
Institut des Matériaux de Nantes
Université de Nantes
UMR 6502, 2 rue de la Houssinière, Nantes 44000, France

The ORCID identification number(s) for the author(s) of this article can be found under https://doi.org/10.1002/admi.202202219.

DOI: 10.1002/admi.202202219

tail group. But a third effect related to the chemical nature of the ligand has to be also considered. The solid/liquid interface could benefit from the chemical properties of the ligands to tune the hydrophilicity, local gas solubility or more generally the interactions between the electrolyte and the catalytic surface. Optimizing the design of organic ligands would then require to distinguish between each contribution of these three effects. In a recent work, Cano and co-workers have employed different capping ligands at gold nanoparticles involved in ORR electrocatalysis.[17] If this work demonstrates the importance of the choice of the ligands, it remains difficult to draw a rationale because, among the four targeted capping ligands, both anchoring and tail groups are simultaneously varied. A more systematic study has been undertaken by Buonsanti et al., here dedicated to CO_2RR process.[18] Interestingly, this work highlights the importance of the tail groups, notably by considering its hydrophobicity for regulating the selectivity of the process.[18] Yet, the hydrophobicity of the ligands is mainly tuned through their tail length, hence contribution of steric geometric effect cannot be ruled out in that case. It turns out that identification of the influence of each effect is challenging and should be carried out with a careful design of ligands.

In this context, we use the versatility of a calix[4]arene platform to explore the influence of the nature of the tail group on the chemical reactivity in ORR electrocatalysis.[19,20] We have recently shown the very good performance of gold nanoparticles functionalized with a monolayer of calix[4]arenes molecules bearing appending carboxyl groups toward ORR in alkaline medium.[21] The calix[4]arenes are grafted at the gold surface through the reductive grafting of diazonium functions that enables a very strong metal–ligand interaction.[22–24] The calix[4]arenes exhibit a cone-constrained structure made of four aromatic units linked by methylene bridges and equipped with four diazonium functions at the large rim. This molecular architecture allows a clean control of the coating at the nanoparticles surface as demonstrated previously.[20,25] Importantly, the small rim of the calix[4]arenes can be easily decorated with various functional groups.[19] Thus, one can vary the length and the chemical nature of the tail groups of ligands which share a common backbone and the same anchoring function. Thanks to this unique molecular design, we are able to focus on the influence of the tail group on the chemical reactivity in ORR. We have then synthesized a series of calix[4]arene-functionalized gold nanoparticles with different functional *termini* including acetic acid, polyethylene glycol, propyl, trifluoro butyl and perfluorinated chains. The choice of these chemical groups is made to vary the length, the hydrophobicity but also the chemical properties (oxygen affinity) of the ligands. The electrocatalytic performances, i.e., efficiency, selectivity and durability are found to be sensitive to the nature of the corresponding tail groups, demonstrating an interplay between length, hydrophobicity and oxygen affinity. Hydrophobicity is a dominant parameter to increase the ORR performances but could be counter-balanced by other chemical properties like oxygen affinity herein. We show that a simple geometric steric consideration relatively to the crowdedness of the ligand, in other words the accessibility at the solid/liquid interface is not enough to predict the chemical reactivity and the chemical properties of the ligands has to be taken into account, providing eventually a fine tool for tuning the reactivity.

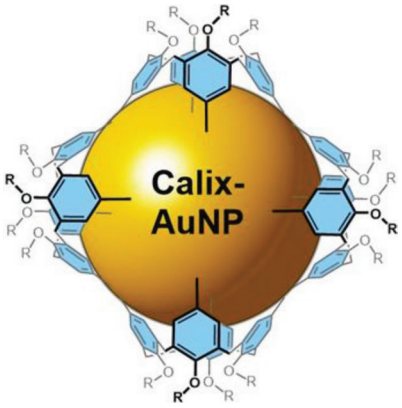

Figure 1. Schematic structure of the hybrid gold nanoparticles. Au-calixCOO$^-$, R = CH_2-COO$^-$; Au-calixPropyl, R = $(CH_2)_2CH_3$; Au-calixCF_3, R = $(CH_2)_3CF_3$; Au-calixC_4F_9, R = $(CH_2)_3C_4F_9$; Au-calixPEG$_4$, R = $CH_2(CH_2OCH_2)_3CH_2OCH_3$.

2. Results and Discussion

2.1. Synthesis of the Hybrid Nanocatalysts

The calix[4]arene-tetradiazonium salts are prepared as previously described.[25–27] Gold nanoparticles are synthesized via a one-pot procedure involving the simultaneous reduction of $HAuCl_4$ and calix[4]arene-tetradiazonium salts with $NaBH_4$ in acetonitrile. This one-step approach has been already described successfully for the preparation of Au-calixCOO$^-$,[25] while it is here reported for the first time for the other calixarene-functionalized nanoparticles, i.e., Au-calixCF_3, Au-calixC_4F_9, Au-calixPEG$_4$, and Au-calixPropyl (**Figure 1**).

Aurate salts and calix[4]arene-tetradiazonium cations are respectively transformed to gold clusters and aryl radicals upon the addition of the reducing agent $NaBH_4$. The calix[4]arene radicals serve as stabilizing agents and their grafting onto the metallic core inhibits the growth of the metal clusters.[28] Thus, the resulting nanoparticles with the calix[4]arene compounds having different terminal groups exhibit close core sizes as evaluated from transmission electronic microscopy (TEM) images after centrifugation and washing cycles (**Figure 2**). We have found 6.1 ± 1.9, 6.5 ± 2.5, 6.4 ± 1.8, 7.8 ± 1.5, and 6.8 ± 1.2 nm for Au-calixCOO$^-$, Au-calixCF_3, Au-calixC_4F_9, Au-calixPEG$_4$ and Au-calixPropyl respectively (Figure S1, Supporting Information). The nanoparticles were dispersed in different solvents, regarding the nature of their terminal groups at the small rim, namely water, acetone, toluene and acetonitrile for Au-calixCOO$^-$, Au-calixCF_3, Au-calixPropyl, Au-calixC_4F_9, and Au-CalixPEG$_4$, respectively. All colloidal suspensions display the characteristic red-ruby color for spherical nanoparticles in agreement with their localized plasmon resonance bands at λ_{max} = 512–528 nm (Figure S2, Supporting Information). The colloidal suspension of Au-calixPropyl is weakly stable and precipitation of the nanoparticles quickly occurs. This precludes any analysis in solution. However, re-homogenization by vigorous stirring is always possible, allowing further characterization and use of deposited nanoparticles. TEM analysis confirms that all the gold nanoparticles are in a spherical shape and well dispersed (Figure 2). In the case of Au-calixC_4F_9, some clusters of nanoparticles can be

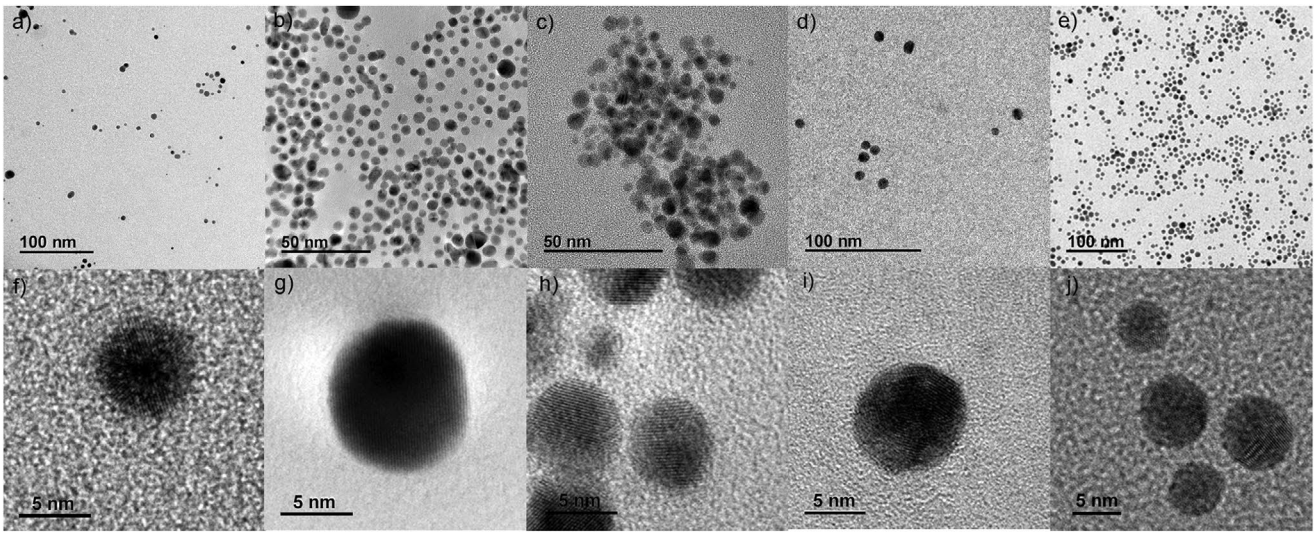

Figure 2. TEM micrographs of a,f) Au-calixCOO$^-$, b,g) Au-calixCF_3, c,h) Au-calixC_4F_9, d,i) Au-calixPEG_4, and e,j) Au-calixPropyl.

observed on the TEM micrograph. They are likely to be due to the entanglement of the polyfluorinated chains of the organic ligands since no irreversible aggregation is observed in the solution.[26]

X-Ray photoelectrons spectroscopy (XPS) measurements are further performed to analyze the surface composition of the nanohybrids which are deposited onto a silicon substrate. **Figure 3** displays the high-resolution core level spectra of Au4f and C1s region. The binding energies for Au4f peaks doublet are found in the range 84–84.4 eV for Au $4f_{7/2}$ and 87.7–88.1 eV for Au $4f_{5/2}$. These values match with the expected values for metallic Au, showing the full reduction of the aurate salts. The binding energy shifts observed among the series of Au-calix nanoparticles are not significant (<0.35 eV) and fall in line with the specific structure of the calix[4]arene platforms that share the same anchoring function and scaffold, mitigating possible electron donating/withdrawing effects. Thus, close reduction potentials for the calix[4]arene-tetradiazonium salts have been evidenced in a previous work.[29] The electronic contribution due to the ligands grafting to the ORR reactivity is then supposed to be of the same order within the Au-calix series. The C1s spectra can be peak-fitted according to several characteristic components that agree well with the different calix[4]arene structures (see table S1, Supporting Information). The calix[4]arene-grafted nanoparticles are excellent candidates to focus only on the nature of the ligand tail toward the ORR reactivity.

Thermogravimetric analysis (TGA) experiments are performed to evaluate the grafting density of calixarenes onto the gold nanoparticles (Figure S3, Supporting Information). The densities calculated from these experiments range from 2 to 3.9 calixarenes nm^{-2} for Au-calixCOO$^-$, Au-calixCF_3, Au-calixPEG_4, and Au-calixPropyl while a higher value is found (≈6.2 calixarenes nm^{-2}) for Au-calixC_4F_9 (Table S2, Supporting Information). It can be noticed that the smallest value is obtained with the colloids that are the easiest to wash, i.e., Au-calixCOO$^-$, readily dispersible in aqueous solution thanks to electrostatic repulsion driven by the carboxylate groups. However, all the obtained densities are indeed larger than the one previously found for calix[4]arene grafted onto flat surfaces (≈0.5–0.6 calixarenes nm^{-2}).[20] The larger curvature of the particle surface is likely to allow denser grafting as previously evidenced.[25] On the other hand, loose ungrafted calix[4]arenes molecules may also contribute to overestimate the grafting densities, since the larger values are obtained with the nanoparticles that are the most difficult to wash. Notably, Au-calixC_4F_9 exhibits the largest grafting density which might account for the entanglement of the polyfluorinated chains, making it difficult to remove all the ungrafted ligands.[26] Nevertheless, the combination of TEM, XPS, and TGA analyses indicate that we have obtained gold nanoparticles of close core size, decorated with roughly a monolayer of calixarenes exhibiting terminal groups of different chemical nature. The functionalized nanoparticles are re-concentrated by centrifugation to be further deposited at the surface of a rotating ring-disk electrode (RRDE) with the same gold mass loading (300 µg cm^{-2}).

2.2. Electrocatalytic Activity toward ORR

The ORR electrocatalytic activities of all the Au-calix nanohybrids are measured using a Pt ring/GC disk rotating ring-disk electrode (RRDE) in O_2-saturated aqueous 0.1 M KOH. The nanomaterials are simply deposited onto the GC surface and covered with Nafion to ensure good mechanical stability at the electrode surface. No supporting carbon is herein employed to disperse the nanoparticles to focus only on the impact of the organic functionalization against the particle itself. It is known that small gold nanoparticles are well-performing catalysts for ORR, mainly through a $2e^- + 2e^-$ pathway.[30–32] O_2 is first reduced to hydroperoxide anion (HO_2^-) (Equation (1)). This hydroperoxide ion can further be reduced to hydroxide anions (OH^-) (Equation (2)) or undergoes a disproportionation (Equation (3)). Notice that in the case of a four-electron pathway, the oxygen (O_2) is directly reduced to hydroxides anions (Equation (4)), as usually observed on Pt-based catalysts

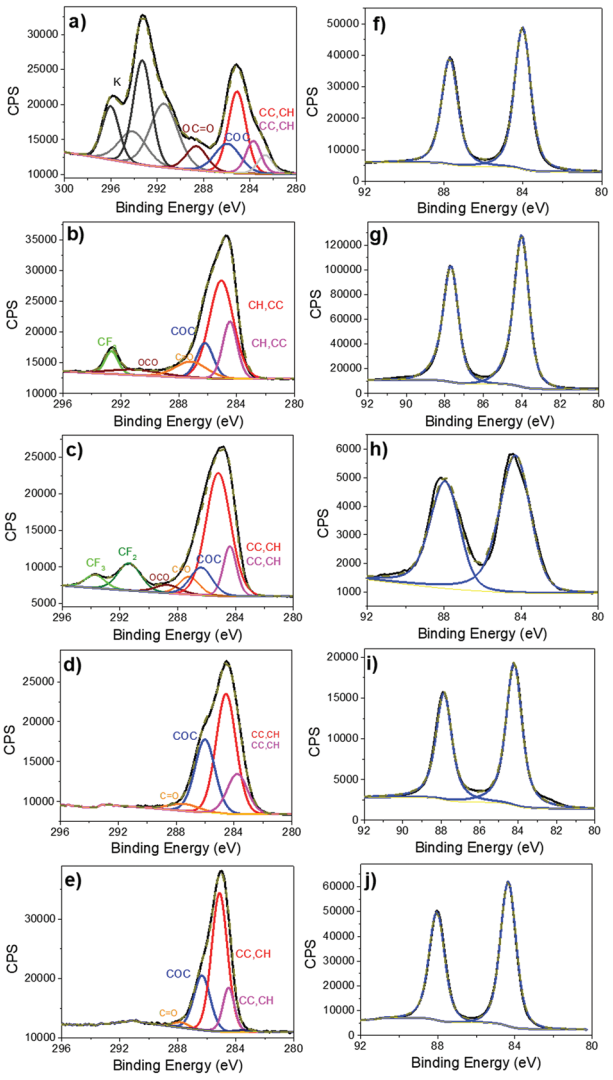

Figure 3. XPS core level spectra for C1s a–e) and Au4f f–j) regions of the calix-decorated gold nanoparticles deposited onto a silicon substrate. a,f) Au-calixCOO$^-$, b,g) Au-calixCF$_3$, c,h) Au-calixC$_4$F$_9$, d,i) Au-calixPEG$_4$, and e,j) Au-calixPropyl.

$$O_2 + H_2O + 2e^- \rightarrow HO_{2^-} + OH^-; E° = -0.076V \text{ vs SHE} \quad (1)$$

$$HO_{2^-} + H_2O + 2e^- \rightarrow 3\,OH^-; E^\circ = 0.878V \text{ vs SHE} \quad (2)$$

$$2HO_{2^-} \rightarrow 2\,OH^- + O_2 \quad (3)$$

$$O_2 + 2\,H_2O + 4e^- \rightarrow 4\,OH^-; E^\circ = 0.401V \text{ vs SHE} \quad (4)$$

Figure 4 displays the typical voltammetries obtained at the disk (bottom curves) and at the ring (top curves) electrodes at ω = 1600 rpm. The whole series can be found in the SI (Figure S4, Supporting Information). The amount of hydroperoxide ions (HO_2^-) possibly produced by the oxygen reduction at the disk electrode is titrated at the Pt ring electrode through its oxidation at 1.70 V versus RHE.

The LSV signals at the disk exhibit the characteristic two-wave polarization curves patterns usually observed at gold

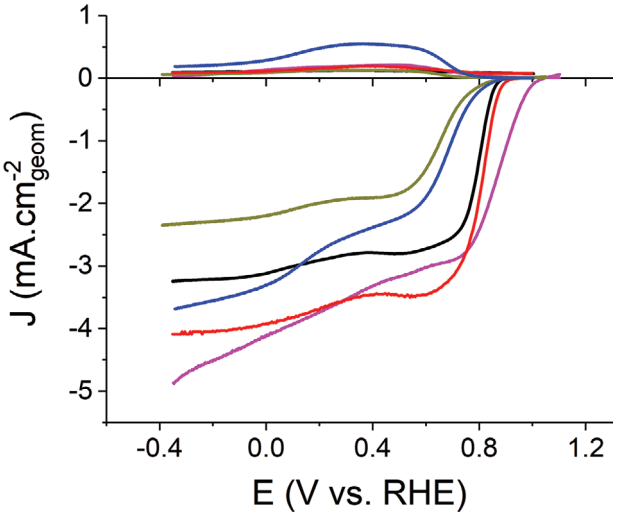

Figure 4. RRDE voltammetric curves in O_2-saturated 0.1 M KOH of GC disk electrodes modified with Au-calixCOO$^-$ (—), Au-calixPEG$_4$ (—), Au-calixPropyl (—), Au-calixCF$_3$ (—), and Au-calixC$_4$F$_9$ (—) (bottom curves) and of Pt ring electrode (top curves). ν = 10 mV s^{-1}, ω = 1600 rpm, E_{ring} = 1.70 V versus RHE.

nanocatalysts, in line with the 2e$^-$ + 2e$^-$ pathway.[21] The half-wave potentials vary with the nature of the tail groups at the calix[4]arenes small rim (**Table 1**). The onset potentials range from 0.99 V (Au-calixPEG$_4$) to 0.79 V (Au-calixPropyl). The tail groups of calix[4]arene functionalizing the gold nanoparticles have different lengths, from shortest ones (calixCOO$^-$ and calixPropyl) to longest one (calixPEG$_4$), and give different wetting properties to the corresponding modified surfaces(Table 1). Contact angle measurements have been performed in previous works with flat gold surfaces, [20,26,27] and showed that the hydrophilicity of the materials varies in the order Au-calixPEG$_4$ > Au-calixCOO$^-$ > Au-calixPropyl > Au-calixCF$_3$ > Au-calixC$_4$F$_9$. We observe that the potential values are impacted by the hydrophilicity of the *termini* rather than by its tail length. Except with Au-calixCF$_3$, the trend suggests that the more hydrophilic terminal group, the smaller is the overpotential. In addition, one can note that the onset or half-wave potential values are comparable than those displayed by other metallic catalysts (Pt, Pd, or Au) being carbon supported,[33–41] or not.[17,42,43] They can be even significantly shifted to more positive potentials in the case of Au-calixPEG$_4$, Au-calixCOO$^-$, and Au-calixCF$_3$. The electrochemical surface area (ECSA) is calculated based on oxides reduction current integration from cyclic voltammetries recorded in an Ar-saturated 0.1 M HClO$_4$ solution (Figure S5, Supporting Information). The ECSA values show a monotonic variation with the interfacial hydrophilicity according to ECSA (Au-calixPEG$_4$) > ECSA (Au-calixCOO$^-$) > ECSA (Au-calixPropyl) > ECSA (Au-calixCF$_3$) > ECSA (Au-calixC$_4$F$_9$). The Au-calixC$_4$F$_9$ exhibit a strong blocking character, probably due to the interaction between the perfluorinated chains, either intra- or intermolecular, that could prevent the access of the aqueous electrolyte to the gold surface.

The quantitative comparison of the efficiency of the nanocatalysts is performed through the analysis of the kinetic current density (J_k) and of the mass activity (kinetic current normalized

Table 1. Contact angle of calix[4]arene-modified gold surfaces, estimation of tail length and electrocatalytic parameters for ORR on the different nanocatalysts in 0.1 M KOH, $\omega = 1600$ rpm.

	Au- calixPEG$_4$	Au- calixCOO$^-$	Au- calixPropyl	Au- calixCF$_3$	Au- calixC$_4$F$_9$
Contact angle	55 ± 5°[a)]	68 ± 3°[b)]	78 ± 3°[b)]	89 ± 2°[b)]	114 ± 3°[c)]
Tail length (Å)[d)]	16.1	3.6	3.9	5.1	9.5
$E_{1/2}$ (V vs RHE)	0.88	0.81	0.65	0.82	0.63
ECSA ($m^2\ g^{-1}_{Au}$)	5.62	1.98	1.07	0.52	0.009
$J_k@E_{1/2}$ ($mA\ cm^{-2}$)	4.1	1.7	1.1	2.3	1.3
MA@$E_{1/2}$ ($A\ g^{-1}_{Au}$)	13.8	6.3	3.7	7.7	4.4
$n(-0.35 < E < E_{onset})$	3.95–3.8	3.9	3.9–3.8	3.9–3.8	3.8–3.2
Max.[e)] % HO_2^-	11	5	5	10	42

[a)]From ref. [27]; [b)]From ref. [20]; [c)]From ref. [26]; [d)]Estimated from MM2 energy minimization with ChemBio3D software; [e)]Taking into account the different values determined for E_{onset} or $E_{1/2}$ for the different catalysts, we have considered the maximum yield production of H_2O^- in the mass-transport-controlled region.

by the Au mass). The kinetic current density is evaluated by the classical Koutecký–Levich analysis at the half-wave potential in the rotating disk electrode experiments to correct mass transfer (Figure S7, Supporting Information). J_k and MA hence formally correspond to the kinetic activity of the nanocatalysts at infinite mass transport. Here again, J_k and MA are much more influenced by the hydrophilic nature of the calix[4]arene tail than by their length (Table 1). Still with the notable exception of Au-calixCF$_3$, the intrinsic catalytic efficiency of the nanocatalysts is enhanced for the most hydrophilic systems (**Figure 5**).

Mass-transfer corrected Tafel plots are constructed to determine the corresponding Tafel slopes (Figure S8, Supporting Information).The Tafel plots display two linear segments of different slopes, as classically reported.[44–46] This slope discontinuity observed between low current density (J)/low overpotential and high current density (J)/high overpotential is still discussed and could originate from a change in the reaction mechanism. Herein, at low J, the absolute Tafel slopes are found to be equal to 50 mV dec^{-1} for Au-calixPEG$_4$, 42 mV dec^{-1} for Au-calixCOO$^-$, 55 mV dec^{-1} for Au-calixPropyl, 49 mV dec^{-1} for Au-calixCF$_3$ and 56 mV dec^{-1} for Au calixC$_4$F$_9$ (Figure S8, Supporting Information). These values are rather close to the typical absolute slope of 60 mV dec^{-1} generally found at low J. Such values could correspond to a pseudo two-electron transfer mechanism where the rate-determining step is the O—O bond breaking.[47] However, the change of the Tafel slopes, and especially the value of 60 mV dec^{-1} has been also proposed to be more likely due to adsorbed species that could alter the kinetics.[45,46,48] For Au-calixPEG$_4$, Au-calixCOO$^-$, and Au-calixCF$_3$, the absolute Tafel slopes are even lower than 60 mV dec^{-1}, notably for Au-calixCOO$^-$ as discussed previously.[21] At higher current density, the Tafel plots exhibit a linear segment with similar slopes of 120 ± 3 mV dec^{-1} for all the Au-calix[4]arene nanocatalysts. This indicates a classical mechanism with no adsorbates other than ORR intermediates where the rate-determining step is the first electron transfer to O_2.[45,49,50] Importantly, the Tafel analysis shows that the mechanism of the ORR is the same for all the studied nanocatalysts, in line with the classically ORR reported pathway.

From the RRDE voltammograms, the number of exchanged electron (n) and hydroperoxide percent yield have been extracted and monitored as a function of potential (**Figure 6**). For all the catalysts, the ORR exhibits behaviors that are in fair agreement with a 2e$^-$ + 2e$^-$ reduction pathway with HO_2^- as intermediates. HO_2^- is first formed then can undergo a further reduction to OH^- at more negative potentials thanks to the good disproportionation activity of gold nanomaterials.[32,39] However, sharp differences can be pointed out among the different nanocatalysts. For Au-calixCOO$^-$, Au-calixPropyl, Au-calixPEG$_4$ and Au-calixCF$_3$, a low production of HO_2^- (≤11%)

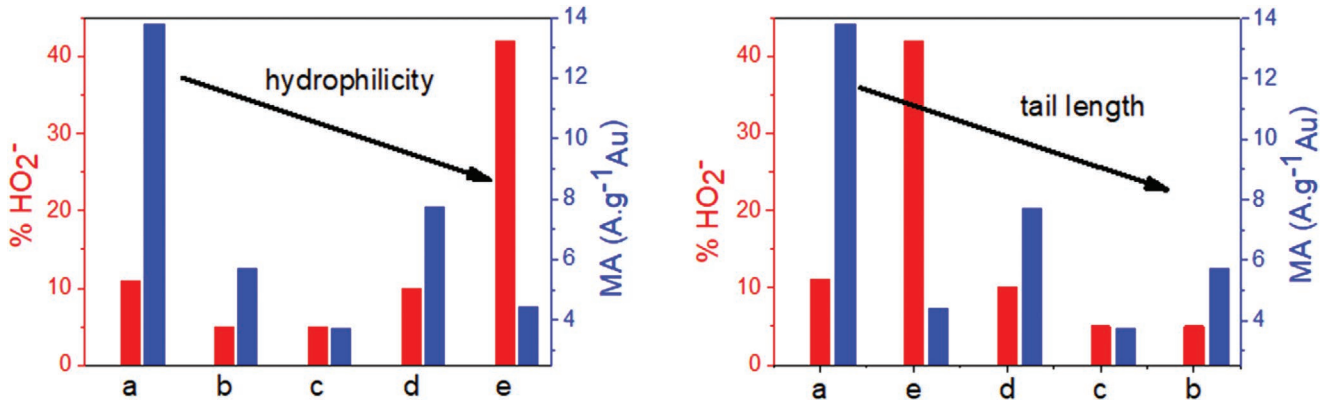

Figure 5. Effect of tail groups on the kinetic mass activity (MA) and maximum amount of hydroperoxide anions (%HO_2^-) that are produced during the ORR process. a) Au-calixPEG$_4$, b) Au-calixCOO$^-$, c) Au-calixPropyl, d) Au-calixCF$_3$, and e) Au-calixC$_4$F$_9$ nanocatalysts.

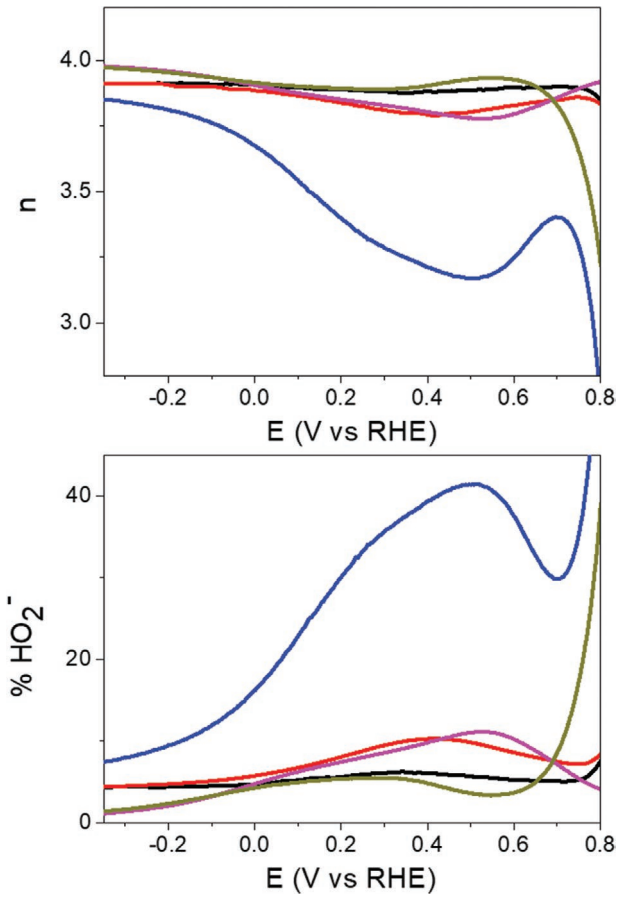

Figure 6. Variation of number of exchanged electrons (n) and yield of HO_2^- produced as a function of potential during ORR experiments in O_2-saturated 0.1 M KOH at the different nanocatalysts (—) Au-calixPEG$_4$, (—) Au-calixCOO$^-$, (—)Au-calixPropyl, (—) Au-calixCF$_3$, and (—) Au-calixC$_4$F$_9$.

is observed with almost no variation of the number of electrons exchanged (3.8–3.95) over the whole potential range (Figure 6 and Table 1). These results indicate a very efficient reduction of HO_2^- to water, suggesting a high selectivity of the reaction with those nanocatalysts since the fraction of HO_2^- produced in the reaction could be seen as an indicator of the selectivity of the reaction. The amount of HO_2^- is even little lower for Au-calixPropyl and Au-calixCOO$^-$, which exhibit a behavior close to that observed for platinum catalysts in acidic media. Note that these features are quite unique for Au electrocatalysts.[43,51,52] Some Au single crystals with (100) facets exhibit remarkable catalytic activity with a 4-e- reaction with almost no production of HO_2^-, albeit in a limited potential range.[53] In contrast, Au-calixC$_4$F$_9$ shows high production of HO_2^- up to 42% while n varies from 3.2 to 3.8 as a function of the potential. Au-COO$^-$ and Au-propyl with the shortest tail show the best selectivity pattern toward the 4-e$^-$ pathway with almost no HO_2^- production, suggesting that the tail length, hence the steric hindrance with respect to the catalytic surface, has an impact on selectivity. However, as for thermodynamic and kinetic efficiencies, the selectivity tends to be much more influenced by the hydrophilicity of the terminal groups than by the length of its tail (Figure 5). Indeed, ORR at Au-PEG$_4$ produces a low amount of HO_2^- despite having the longest tail thanks to its superior hydrophilicity. Importantly, at this stage, it is worth outlining that Au-PEG$_4$ exhibits enhanced performance within the whole series although that its tail length would have led to strong steric effect supposed to hamper the reaction. This result shows that accessibility is not necessarily a key parameter in the process efficiency. Au-calixC$_4$F$_9$ which is the most hydrophobic material leads to high fraction of HO_2^-, although it presents a shorter tail than Au-calixPEG$_4$ (Table 1). On the other hand, we can notice that Au-calixCF$_3$ is systematically outside the trends observed within the series of Au-calix regarding the thermodynamic potentials, mass activity and selectivity. Despite having longer tail and being more hydrophobic, the performances of Au-calixCF$_3$ are approaching those of Au-calixCOO$^-$, but with a smaller ECSA. This observation suggests that the interactions with the surrounding solvent is probably not the sole aspect modulating the catalysts reactivity. The fluorinated tail group may increase the local O_2 concentration allowing better ORR efficacy.[54] However, the interplay between steric hindrance, hydrophobicity and affinity toward O_2 is subtle and a trade-off between all these effects is obviously necessary to increase the performances. Au-calixCF$_3$ is likely to represent the best compromise, explaining its good catalytic activity and selectivity for the 4-e$^-$ pathway. In contrast, despite being equipped with perfluorinated chains, hence having a better affinity with O_2 than Au-calixCF$_3$, Au-calixC$_4$F$_9$ exhibits poorer electrocatalytic performance and selectivity because of its larger hydrophobicity. Nevertheless, an even worse selectivity toward the 4-electron pathway could have been expected from the hydrophobic nature of the C$_4$F$_9$ tail. Indeed, Mirkhalaf and co-workers has demonstrated that gold nanoparticles capped with a monolayer of decylphenyl moieties catalyze the oxygen reduction process to the formation of peroxide (2-e$^-$ process).[55] In this work, the capping ligands are found to establish a local hydrophobic environment that strongly impacts the reaction mechanism.[55] The strong affinity of the perfluorinated chains for oxygenated species in the Au-calixC$_4$F$_9$ is likely to mitigate the effect of the local hydrophobic environment, enabling a moderate but significant efficacy of the 4-e$^-$ conversion of O_2.

2.3. Durability of the Nanocatalysts

Durability of the calix-functionalized Au nanocatalysts is analyzed through a drastic sequence of stability tests. They consist first of one thousand cyclic voltammetries by sweeping the potential between 1.2 and –0.35 V versus RHE in aqueous O_2-saturated 0.1 M KOH at 500 mV s^{-1}. Then the same samples undergo a 12h-chronoamperometry at 0.75 V versus RHE. LSV curves are then recorded and compared with the signals obtained before applying this stability tests sequence (**Figure 7**).

All the nanocatalysts show very good stability, with the highest durability for Au-calixCOO$^-$ and Au-calixPEG$_4$. ECSA are also estimated from cyclic voltammetries before and after the durability tests for the different nanocatalysts except for Au-calixC$_4$F$_9$ which exhibit too small ECSA values to have meaningful variation (Figure S6, Supporting Information). About 60% of Au-calixCOO$^-$ (63%) and Au-calixCF$_3$ (58%) remain electrochemically active after the drastic sequence of stability

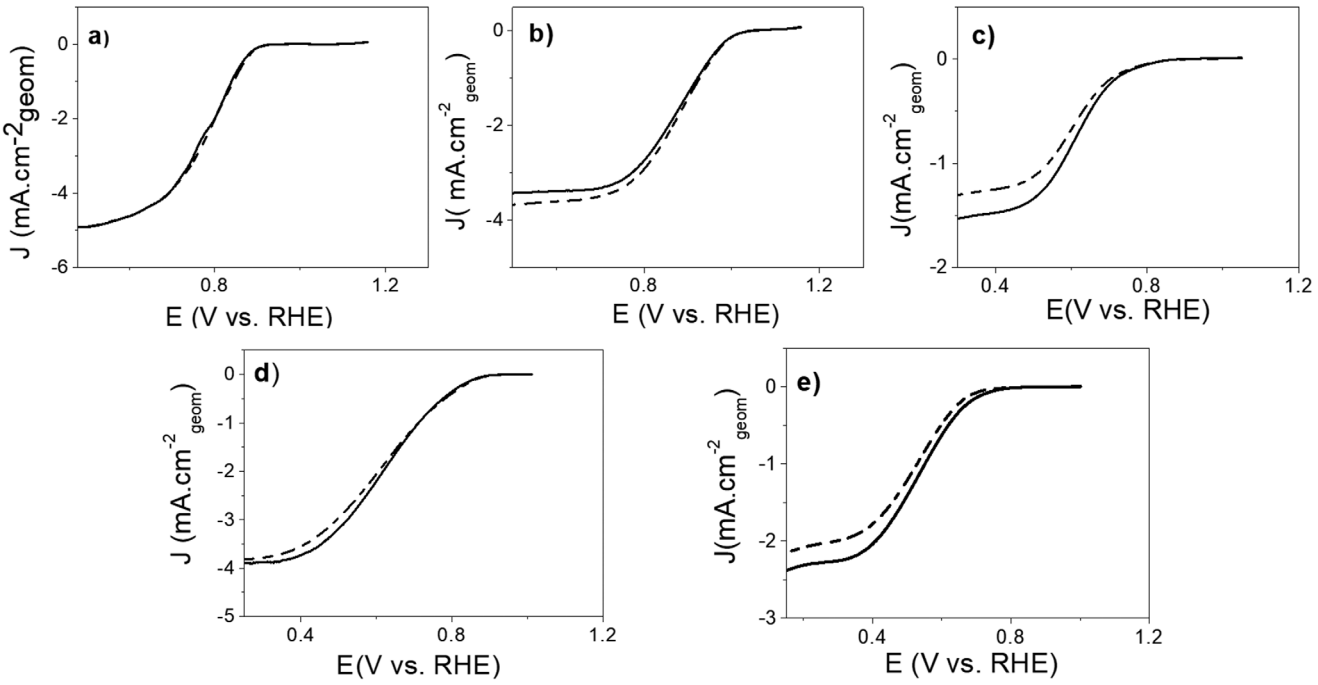

Figure 7. LSV curves in O_2-saturated 0.1 M KOH before (solid line) and after (dashed line) the sequence of stability tests a) Au-calixCOO–, b) Au-calixPEG$_4$ c) Au-calixPropyl, d) Au-calixCF$_3$, and e) Au-calixC$_4$F$_9$. $\omega = 1600$ rpm. $\nu = 10$ mV s^{-1}.

tests (1000 cycles + 12h-chronoamperometry) while even 88% of Au-calixPEG$_4$ is still operative. In contrast, Au-calixPropyl is much more affected and exhibits a 79% loss of ECSA. XPS analyses of the deposits made before and after the stability tests do not reveal significant differences (Figures S9 and S10, Supporting Information). Especially, the core level signals for Au4f remain almost identical for all the nanocatalysts (Figure S9, Supporting Information). The XPS observations suggest that hybrid nanocatalysts remain generally intact in contrast to what we observe with citrate capped gold nanoparticles in a previous work.[21] This also suggests that the hydrophilic and hydrophobic properties of the different nanocatalysts do not change after the catalytic reaction.

3. Conclusion

A series of gold-functionalized nanocatalysts has been synthesized by varying the organic ligands grafted onto the nanoparticles' surface. The organic ligands display an identical architecture based on calix[4]arene platform sharing the same anchoring groups and molecular backbone. Variation of the tail group at the calix[4]arene small rim enables an easy tuning of the solid/liquid interface without changing the nature of the interaction between the metallic surface and the ligand and the spatial distribution of the ligands at the surface. Our results indicate the importance of the nature of the ligand tail in controlling the activity of the gold nanoparticles. Steric effects due to the tail length which it is supposed to regulate the accessibility to catalytic sites are found to have finally little influence. The hydrophilicity is shown to play a much more dominant role in modulating the catalyst performance. The more hydrophilic the ligand, the better the catalyst performance and selectivity is, irrespective of the tail length. Thus the hydrophilic Au-calixPEG$_4$ is favorably competitive to the hydrophilic Au-calixCOO$^-$, despite a much longer tail, hence demonstrating that the chemical nature of the tail outweighs its possible steric hindrance. Furthermore, we show that this wetting properties aspect could even be balanced by the specific chemical properties brought by a given molecular design of the ligand. Thus Au-calixCF$_3$ and Au-calixC$_4$F$_9$ exhibit a much better activity and selectivity toward ORR than could be expected on the basis of their hydrophobicity, owing to their strong affinity to O_2. This work contributes to highlight the interest of functionalizing metal-based nanocatalysts with organic molecules by using molecular chemistry approaches. The chemical properties of a specifically designed organic ligands can promote specific interactions including selective inhibition or second-sphere coordination to enhance catalysts efficiency and selectivity.

4. Experimental Section

Chemicals: Solvents and reagents for the syntheses were at least of reagent grade quality and were used without further purification.

Synthesis: Calix[4]arene functionalized gold nanoparticles were synthesized according to an one-pot procedure. Gold salt $HAuCl_4 \cdot {}_3H_2O$ purchased from Sigma Aldrich (>99.9%) was dissolved in dry acetonitrile (20 mL) and mixed with an acetonitrile solution (20 mL) of calix[4]arene tetradiazonium salts (1 eq.). The reaction mixture was stirred vigorously at 0 °C under Ar and an aqueous solution of $NaBH_4$ (Sigma Aldrich, ≥98%, 0.5 mg in 1 mL) was added dropwise. The color of the reaction mixture changed from yellow to dark ruby. After 2 h of vigorous stirring at room temperature, the reaction mixture was centrifuged at 10 000 rpm for 20 min, resulting in gold nanoparticles functionalized with calix[4] arenes ligands. The nanoparticles were washed 3 times by centrifugation

and re-dispersed in acetonitrile, water, toluene or acetone depending on the nature of the calix[4]arene ligands, with a concentration equal to 2 mg_{Au} mL^{-1}.

Caution! Although we have not encountered any problem, it is noted that diazonium salts derivatives are potentially explosive and should be handled with appropriate precautions.

Transmission Electron Microscopy: Morphology and size distribution of the samples were investigated by high-resolution transmission electron microscopy (HRTEM), using a Jeol 2100 with an acceleration voltage of 200 kV on which the images were recorded on a GATAN Orius 200 CCD camera. The size distribution was estimated using ImageJ software, version 1.52a.

X-Ray Photoelectrons Spectroscopy: XPS data have been collected by a Kratos Axis Nova spectrometer using the Al Kα X-ray source working at 1486.6 eV and using a spot size of 0.7 × 0.3 mm^2. Survey spectra (0–1000 eV) (Figure S7, Supporting Information) were acquired with an analyzer pass energy of 160 eV (0.5 eV/step); high resolution spectra used a pass energy of 40 eV (0.1 eV/step). Binding energies were referenced to C1s peak at 285 eV. The core level spectra were peak-fitted using the CasaXPS Software, Ltd. Version 2.3.18. U2 Tougaard or Shirley was used as background. The peaks areas were normalized by the manufacturer-supplied sensitivity factor ($S_{C1s} = 0.278$, $S_{F1s} = 1$, $S_{O1s} = 0.78$, $S_{S2p} = 0.668$, and $S_{Au4f} = 6.25$). Since the XPS measurements cannot be made with the RRDE electrodes due to their height, deposit of AuNPs were performed onto screen-printed carbon electrode Dropsens. The modified electrodes subsequently underwent ORR stability experiments (1000 cycles at 500 mV s^{-1} from 1.20 to –0.35 V vs RHE) under the same experimental conditions used for ORR measurements with RRDE. For each sample, XPS spectra were recorded on three different locations, and we did not observe any difference.

Thermogravimetric Analyses: The thermogravimetric analyses (TGA) were performed with a TA instruments Model SDT 2960. For this purpose, 4 to 6 mg of dry nanoparticles weighed in a ceramic crucible Perkin Elmer TGA undergo a linear ramp of increasing temperature from 30 to 900 °C at a rate of 10 °C min^{-1} under nitrogen atmosphere. The obtained results are then processed with the TA data analysis software.

Electrochemical Analyses: The ORR activity was evaluated using a rotating Pt/GC ring-disk electrode (37% collection efficiency) controlled by a MSR Rotator from Pine Research. The GC electrode preparation (deposit of catalysts) is described in the supplementary part. The LSV scans were recorded using an Autolab PGSTAT302N potentiostat-galvanostat (Metrohm) equipped with a BIPOT module, in a conventional three-electrode electrochemical cell at a scan rate of 10 mV s^{-1} in a 0.1 M KOH solution saturated with O_2. A platinum grid and an Hg/HgO, (20% KOH) electrode were used as counter and reference electrodes, respectively. Voltammograms were recorded with the Metrohm Nova 2.1 software. The potentials were not corrected from *iR* drop. The potentials are reported against the reversible hydrogen electrode according to $E(\text{RHE}) = E(\text{Hg/HgO}) + 0.059\ \text{pH} + 0.098$.

The number of electrons exchanged can be quantified using the disk and ring currents according to

$$n = \frac{4 I_D}{I_D + \left(\frac{I_R}{N}\right)} \quad (5)$$

where I_D is the modulus of the disk current, I_R is the ring current corresponding to the oxidation of HO_2^-, and N is the collection efficiency. N was determined as 0.37 using the ferro/ferricyanide couple, in agreement with manufacturer indication.[56]

The onset potential E_{onset} was measured on the LSV curves as the potential corresponding to 5/100 of I_L, I_L being the diffusion limiting current.

Surface of electrochemically active AuNPs (ECSA) was measured by cyclic voltammetry at 100 mV s^{-1} in an aqueous 0.1 M $HClO_4$ purged with Ar. Acidic solution is preferred because the gold oxides reduction peak is generally better-resolved in acidic media. A platinum grid and a SCE electrode, KCl (sat.) were used as the counter and reference electrode, respectively. Potential was swept until stabilization of the signal

$$ECSA = \frac{Q_{oxides}}{m \times C} \quad (6)$$

where Q_{oxides} is the charge integrated from the voltammetric peak corresponding to the reduction of gold oxides, m is the mass of gold deposited and C is the monolayer adsorption charge on Au (400 μC cm^{-2}).[57]

Supporting Information

Supporting Information is available from the Wiley Online Library or from the author.

Acknowledgements

This work was supported by Agence Nationale de la Recherche ANR-21-CE50-MARCEL project. Q.L. thanks the French Ministry of Research for financial support. The authors are grateful to L. Rault for the assistance in TEM experiments performed on THEMIS platform (CPER-FEDER 2007-2014). R. Lebullenger (University of Rennes 1) is thanked for his help in the TGA analyses. The authors are indebted to L. Troian-Gautier (ULB) for his help in the synthesis of calixarenes.

Conflict of Interest

I.J. and C.L. are shareholders of X4C. I.J. is a consultant for X4C. All other authors declare that they have no conflict of interest.

Data Availability Statement

The data that support the findings of this study are available from the corresponding author upon reasonable request.

Keywords

diazonium, electrocatalysis, nanoparticles, ORR, surface functionalization

Received: October 13, 2022
Revised: November 29, 2022
Published online: January 19, 2023

[1] M. L. Pegis, C. F. Wise, D. J. Martin, J. M. Mayer, *Chem. Rev.* **2018**, *118*, 2340.
[2] Z.-L. Wang, D. Xu, J.-J. Xu, X.-B. Zhang, *Chem. Soc. Rev.* **2014**, *43*, 7746.
[3] F. Cheng, J. Chen, *Chem. Soc. Rev.* **2012**, *41*, 2172.
[4] H. Mistry, A. S. Varela, S. Kühl, P. Strasser, B. R. Cuenya, *Nat. Rev. Mater.* **2016**, *1*, 16009.
[5] Y. Dai, Y. Wang, B. Liu, Y. Yang, *Small* **2015**, *11*, 268.
[6] M. M. Montemore, M. A. van Spronsen, R. J. Madix, C. M. Friend, *Chem. Rev.* **2018**, *118*, 2816.
[7] L. M. Rossi, J. L. Fiorio, M. A. S. Garcia, C. P. Ferraz, *Dalton Trans.* **2018**, *47*, 5889.
[8] A. R. Tao, S. Habas, P. Yang, *Small* **2008**, *4*, 310.

[9] G. Fu, K. Wu, J. Lin, Y. Tang, Y. Chen, Y. Zhou, T. Lu, *J. Phys. Chem. C* **2013**, *117*, 9826.
[10] D. Y. Chung, S. W. Jun, G. Yoon, S. G. Kwon, D. Y. Shin, P. Seo, J. M. Yoo, H. Shin, Y.-H. Chung, H. Kim, B. S. Mun, K.-S. Lee, N.-S. Lee, S. J. Yoo, D.-H. Lim, K. Kang, Y.-E. Sung, T. Hyeon, *J. Am. Chem. Soc.* **2015**, *137*, 15478.
[11] X.-Y. Lang, G.-F. Han, B.-B. Xiao, L. Gu, Z.-Z. Yang, Z. Wen, Y.-F. Zhu, M. Zhao, J.-C. Li, Q. Jiang, *Adv. Funct. Mater.* **2015**, *25*, 230.
[12] Y. J. Tong, *Chem. Soc. Rev.* **2012**, *41*, 8195.
[13] J. Wang, F. Zhang, X. Kang, S. Chen, *Curr. Opinion Electrochem.* **2019**, *13*, 40.
[14] Q. Lenne, Y. R. Leroux, C. Lagrost, *ChemElectroChem* **2020**, *7*, 2345.
[15] D.-H. Nam, P. De Luna, A. Rosas-Hernández, A. Thevenon, F. Li, T. Agapie, J. C. Peters, O. Shekhah, M. Eddaoudi, E. H. Sargent, *Nat. Mater.* **2020**, *19*, 266.
[16] L. Lu, S. Zou, B. Fang, *ACS Catal.* **2021**, *11*, 6020.
[17] D. Alba-Molina, A. R. Puente Santiago, J. J. Giner-Casares, E. Rodríguez-Castellón, M. T. Martín-Romero, L. Camacho, R. Luque, M. Cano, *J. Mat. Chem. A* **2019**, *7*, 20425.
[18] J. R. Pankhurst, Y. T. Guntern, M. Mensi, R. Buonsanti, *Chem. Sci.* **2019**, *10*, 10356.
[19] L. Troian-Gautier, A. Mattiuzzi, O. Reinaud, C. Lagrost, I. Jabin, *Org. Biomol. Chem.* **2020**, *18*, 3624.
[20] A. Mattiuzzi, I. Jabin, C. Mangeney, C. Roux, O. Reinaud, L. Santos, J.-F. Bergamini, P. Hapiot, C. Lagrost, *Nat. Commun.* **2012**, *3*, 1130.
[21] Q. Lenne, A. Mattiuzzi, I. Jabin, N. L.E Poul, Y. R. Leroux, C. Lagrost, *Adv. Mater. Interfaces* **2020**, *7*, 2001557.
[22] J. Pinson, F. Podvorica, *Chem. Soc. Rev.* **2005**, *34*, 429.
[23] D. Bélanger, J. Pinson, *Chem. Soc. Rev.* **2011**, *40*, 3995.
[24] A. A. Mohamed, Z. Salmi, S. A. Dahoumane, A. Mekki, B. Carbonnier, M. M. Chehimi, *Adv. Colloid Interface Sci.* **2015**, *225*, 16.
[25] L. Troian-Gautier, H. Valkenier, A. Mattiuzzi, I. Jabin, N. V. den Brande, B. V. Mele, J. Hubert, F. Reniers, G. Bruylants, C. Lagrost, Y. Leroux, *Chem. Commun.* **2016**, *52*, 10493.
[26] A. Mattiuzzi, L. Troian-Gautier, J. Mertens, F. Reniers, J.-F. Bergamini, Q. Lenne, C. Lagrost, I. Jabin, *RSC Adv.* **2020**, *10*, 13553.
[27] P. Blond, A. Mattiuzzi, H. Valkenier, L. Troian-Gautier, J.-F. Bergamini, T. Doneux, E. Goormaghtigh, V. Raussens, I. Jabin, *Langmuir* **2018**, *34*, 6021.
[28] F. Mirkhalaf, J. Paprotny, D. J. Schiffrin, *J. Am. Chem. Soc.* **2006**, *128*, 7400.
[29] L. Santos, A. Mattiuzzi, I. Jabin, N. Vandencasteele, F. Reniers, O. Reinaud, P. Hapiot, S. Lhenry, Y. Leroux, C. Lagrost, *J. Phys. Chem. C* **2014**, *118*, 15919.
[30] M. S. El- Deab, T. Ohsaka, *Electrochem. Commun.* **2002**, *4*, 288.
[31] M. S. El-Deab, T. Ohsaka, *Electrochim. Acta* **2002**, *47*, 4255.
[32] P. Rodriguez, M. T. M. Koper, *Phys. Chem. Chem. Phys.* **2014**, *16*, 13583.
[33] C. N. Kostelansky, J. J. Pietron, M.-S. Chen, W. J. Dressick, K. E. Swider-Lyons, D. E. Ramaker, R. M. Stroud, C. A. Klug, B. S. Zelakiewicz, T. L. Schull, *J. Phys. Chem. B* **2006**, *110*, 21487.
[34] J. E. Newton, J. A. Preece, N. V. Rees, S. L. Horswell, *Phys. Chem. Chem. Phys.* **2014**, *16*, 11435.
[35] P. Joshi, T. Okada, K. Miyabayashi, M. Miyake, *Anal. Chem.* **2018**, *90*, 6116.
[36] K. Miyabayashi, H. Nishihara, M. Miyake, *Langmuir* **2014**, *30*, 2936.
[37] Z.-Y. Zhou, X. Kang, Y. Song, S. Chen, *Chem. Commun.* **2012**, *48*, 3391.
[38] L. Jiang, A. Hsu, D. Chu, R. Chen, *J. Electrochem. Soc.* **2009**, *156*, B643.
[39] H. Erikson, G. Jürmann, A. Sarapuu, R. J. Potter, K. Tammeveski, *Electrochim. Acta* **2009**, *54*, 7483.
[40] H. Yin, H. Tang, D. Wang, Y. Gao, Z. Tang, *ACS Nano* **2012**, *6*, 8288.
[41] H. Erikson, A. Sarapuu, K. Tammeveski, J. Solla-Gullón, J. M. Feliu, *ChemElectroChem* **2014**, *1*, 1338.
[42] I. Srejic, Z. Rakocevic, M. Nenadovic, S. Strbac, *Electrochim. Acta* **2015**, *169*, 22.
[43] W. Tang, H. Lin, A. Kleiman-Shwarsctein, G. D. Stucky, E. W. McFarland, *J. Phys. Chem. C* **2008**, *112*, 10515.
[44] D. B. Sepa, M. V. Vojnovic, A. Damjanovic, *Electrochim. Acta* **1981**, *26*, 781.
[45] J. X. Wang, N. M. Markovic, R. R. Adzic, *J. Phys. Chem. B* **2004**, *108*, 4127.
[46] K. J. J. Mayrhofer, B. B. Blizanac, M. Arenz, V. R. Stamenkovic, P. N. Ross, N. M. Markovic, *J. Phys. Chem. B* **2005**, *109*, 14433.
[47] H. A. Hansen, V. Viswanathan, J. K. Nørskov, *J. Phys. Chem. C* **2014**, *118*, 6706.
[48] A. Holewinski, S. Linic, *J. Electrochem. Soc.* **2012**, *159*, H864.
[49] R. W. Zurilla, R. K. Sen, E. Yeager, *J. Electrochem. Soc.* **1978**, *125*, 1103.
[50] T. Shinagawa, A. T. Garcia-Esparza, K. Takanabe, *Sci. Rep.* **2015**, *5*, 13801.
[51] D. Alba-Molina, A. R. Puente Santiago, J. J. Giner-Casares, M. T. Martín-Romero, L. Camacho, R. Luque, M. Cano, *J. Phys. Chem. C* **2019**, *123*, 9807.
[52] L. Wang, Z. Tang, W. Yan, H. Yang, Q. Wang, S. Chen, *ACS Appl. Mater. Interfaces* **2016**, *8*, 20635.
[53] R. R. Adžić, S. Strbac, N. Anastasijević, *Mater. Chem. Phys.* **1989**, *22*, 349.
[54] K. Miyabayashi, M. Miyake, *Electroanalysis* **2017**, *29*, 898.
[55] F. Mirkhalaf, D. J. Schiffrin, *Langmuir* **2010**, *26*, 14995.
[56] E. Claude, T. Addou, J. M. Latour, P. Aldebert, *J. Appl. Electrochem.* **1998**, *28*, 57.
[57] B. Piela, P. K. Wrona, *J. Electroanal. Chem.* **1995**, *388*, 69.